

Contents lists available at ScienceDirect

Journal of Energy Chemistry

journal homepage: www.elsevier.com/locate/jechem



http://www.journals.elsevier.com/

Operando X-ray diffraction analysis of the degradation mechanisms of a spinel LiMn₂O₄ cathode in different voltage windows

Fakui Luo^{a,1}, Congcong Wei^{a,1}, Chi Zhang^b, Hui Gao^a, Jiazheng Niu^a, Wensheng Ma^a, Zhangquan Peng^{b,c}, Yanwen Bai^{a,*}, Zhonghua Zhang^{a,b,**}

- ^a Key Laboratory for Liquid-Solid Structural Evolution and Processing of Materials (Ministry of Education), School of Materials Science and Engineering, Shandong University, Jingshi Road 17923, Jinan 250061, Shandong, China
- ^b School of Applied Physics and Materials, Wuyi University, 22 Dongcheng Village, Jiangmen 529020, Guangdong, China
- ^c State Key Laboratory of Electroanalytical Chemistry, Changchun Institute of Applied Chemistry, Chinese Academy of Sciences, Changchun 130022, Jilin, China

ARTICLE INFO

Article history: Received 3 July 2019 Revised 8 September 2019 Accepted 13 September 2019 Available online 19 September 2019

Keywords: Lithium-ion battery Over-discharge Phase transition Cathode Operando X-ray diffraction

ABSTRACT

The understanding of reaction mechanisms of electrode materials is of significant importance for the development of advanced batteries. The LiMn₂O₄ cathode has a voltage plateau around 2.8 V (vs. Li⁺/Li), which can provide an additional capacity for Li storage, but it suffers from a severe capacity degradation. In this study, operando X-ray diffraction is carried out to investigate the structural evolutions and degradation mechanisms of LiMn₂O₄ in different voltage ranges. In the range of 3.0–4.3 V (vs. Li⁺/Li), the LiMn₂O₄ cathode exhibits a low capacity but good cycling stability with cycles up to 100 cycles and the charge/discharge processes are associated with the reversible extraction/insertion of Li⁺ from/into Li_xMn₂O₄ (0 \leq x \leq 1). In the range of 1.4–4.4 V (vs. Li⁺/Li), a capacity higher than 200 mAh/g is achieved, but it rapidly decays during the cycling. The voltage plateau around 2.8 V (vs. Li⁺/Li) is related to the transformation of the cubic LiMn₂O₄ phase to the tetragonal Li₂Mn₂O₄ phase, which leads to the formation of cracks as well as the performance degradation.

© 2019 Science Press and Dalian Institute of Chemical Physics, Chinese Academy of Sciences. Published by Elsevier B.V. and Science Press. All rights reserved.

1. Introduction

The state-of-the-art lithium-ion battery (LIB) technologies have been successfully employed in various applications, such as portable electronics, electric vehicles, hybrid electric vehicles, and grid energy storage [1,2]. Among the cathode materials currently used in LIBs, spinel LiMn₂O₄ has a high market share because of its unique advantages of cost effectiveness and environmental friendliness [3]. Generally, the operation voltage range of the commercialized LiMn₂O₄ cathode material is set to 3.0–4.3 V (vs. Li⁺/Li). In this voltage range, the spinel LiMn₂O₄ cathode exhibits a voltage plateau around 4.1 V (vs. Li⁺/Li), which corresponds to

the $Mn^{3.5+}/Mn^{4+}$ redox reaction [4]. However, $LiMn_2O_4$ exhibits another voltage plateau around 3.0 V (vs. Li^+/Li), associated with the $Mn^{3+}/Mn^{3.5+}$ redox reaction and formation of $Li_2Mn_2O_4$ [5]. $Li_2Mn_2O_4$ can deliver a high theoretical specific capacity of 285.5 mAh/g, which is approximately twice that of $LiMn_2O_4$ (148.2 mAh/g). However, the valence state of the manganese ion below +3.5 accelerates the capacity fading, which can be attributed to the Jahn–Teller effect [6,7], corrosion and dissolution of the cathode material [8], phase transitions, and local structure inhomogeneity [9].

In addition, the mechanical degradation is another reason for capacity fading of the cathode. Intergranular cracks originated from the volume changes during the charging/discharging have been observed and correlated with the capacity fading [10–12]. The intergranular cracks lead to poor grain-to-grain connections and enhance the side reactions, which hinders the electronic and ionic transports, and thereby decreases the reversibility [13]. Intragranular cracks with a high density but small sizes also lead to a capacity loss [14]. A systematic investigation on the relationship between intergranular and intragranular cracks in cathode materials is still lacking. Various approaches can be used to mitigate the

^{*} Corresponding author.

^{**} Corresponding authors at: Key Laboratory for Liquid-Solid Structural Evolution and Processing of Materials (Ministry of Education), School of Materials Science and Engineering, Shandong University, Jingshi Road 17923, Jinan 250061, Shandong, China

E-mail addresses: bai_yanwen@163.com (Y. Bai), zh_zhang@sdu.edu.cn (Z. Zhang).

¹ These authors contributed equally to this work.

crack formation. For example, a surface coating can prevent intergranular cracking while mitigation of the intragranular cracking requires a stable structural framework [14]. However, the mechanical degradation of the cathode can hardly be detected or quantified synchronously during the charging/discharging. Postmortem technologies, such as ex-situ X-ray diffraction (XRD) [15-18], scanning electron microscopy (SEM) [19,20], and transmission electron microscopy (TEM) [21], have been extensively utilized to investigate the degradation. Nevertheless, the structures and properties of electrode materials change when they are removed from the cells and exposed to air. For example, $Li_2Mn_2O_4$ is not stable in air [22]. To avoid these drawbacks, operando (in-situ) analytic methods are utilized, such as operando TEM [12,23], operando XRD [24,25], and operando X-ray absorption near-edge-structure spectroscopy [26]. Among these operando techniques, XRD can be used to identify the phase composition, lattice parameters, and atomic ordering. It is of importance to probe the capacity degradation mechanisms of the LiMn₂O₄ cathode in different voltage ranges by using operando techniques, such as the operando XRD.

In this study, we investigated the dependence of the electrochemical performance of a spinel LiMn_2O_4 cathode on the voltage window. The degradation mechanisms of LiMn_2O_4 were further analyzed by using operando XRD. The phase transition from the cubic LiMn_2O_4 to the tetragonal $\text{Li}_2\text{Mn}_2\text{O}_4$ accounts for the performance decay in the voltage window with the discharge plateau around 2.8 V (vs. Li^+/Li).

2. Experimental

2.1. Microstructural characterization

The LiMn $_2$ O $_4$ sample was purchased from Kejing Materials Technology Co. Ltd., Hefei, China. The phase constitution of the asprepared sample was identified by XRD (Beijing Purkinje General Instrument Co. Ltd, China) with Cu K_{α} radiation. The morphology of the obtained sample was characterized by SEM (ZEISS SIGMA 300).

2.2. Electrochemical measurements

The electrode was prepared by mixing the active material, acetylene black (Super P), and polyvinylidene fluoride in a weight ratio of 70:20:10. The slurry was painted on an Al foil, and then dried at 120 °C in vacuum for 12 h. The painted Al foil was punched into an electrode with a diameter of 12 mm and loading of 0.8-1.2 mg. A CR2032 cell was assembled in an argon-filled glove box with the LiMn₂O₄ electrode as the working electrode, Li foil as the counter/reference electrode, polypropylene septum (Celgard 2325) as the separator, and 1 M of LiPF₆ in a solvent of 3:7 ethyl carbonate/dimethyl carbonate as the electrolyte. Cyclic voltammetry (CV) measurements were carried out at a scan rate of 0.1 mV/s by using a CHI660E potentiostat. A test system (LAND-CT2001A, Wuhan, China) was used to perform galvanostatic tests in the voltage ranges of 3.0-4.3 and 1.4-4.4V (vs. Li+/Li) at a constant temperature of 30 °C. After cycling, some cells were disassembled in the glove box, and the $LiMn_2O_4$ electrodes were washed and dried for ex-situ SEM observations. For the operando XRD measurements, the LiMn₂O₄ cathode slurry was painted on a stainless-steel mesh (thickness: 0.1 mm). The XRD signals were collected through the beryllium window of the coin cell in the "time step" mode during the charging/discharging at a current density of 20 mA/g. Additionally, a Rietveld refinement and indexing were performed by using the Reflex suite in Materials Studio (MS, version 7.0) of Accelrys Inc.

3. Results and discussion

Fig. 1(a) shows the XRD pattern and Rietveld refinement results for the LiMn₂O₄. The Rietveld refinement of the sample converges to a cubic unit cell (space group: Fd3m) with a=b=c=8.248 Å, which is consistent with the data for cubic LiMn₂O₄ in the Inorganic Crystal Structure Database (ICSD #50,427). The inset of Fig. 1(a) illustrates the crystal structure of LiMn₂O₄ with a framework connected by MnO₆ octahedrons. Li, Mn, and O ions occupy 8a, 16d, and 32e lattice sites in the LiMn₂O₄ structure, respectively. The Rietveld refinement results with a weighted profile R factor ($R_{\rm wp}$) of 12.60% indicate that the main heavy atoms of the structure are correctly positioned. Figs. 1(b) and S1 show typical SEM images of the LiMn₂O₄ at different magnifications, which indicate that the particles are polyhedrons with sizes in the range of 100 nm to 1 μ m.

Fig. 2(a) shows typical CV curves of $LiMn_2O_4$ at $0.1\,mV/s$ in the voltage range of 3.0-4.3 V (vs. Li+/Li). The oxidation peaks at 4.05 and 4.17 V (vs. Li⁺/Li) correspond to the two-stage conversion of the $LiMn_2O_4$ phase to the $Li_xMn_2O_4$ ($0 \le x \le 1$) phase, while the reduction peaks at 3.97 and 4.11 V (vs. Li+/Li) are associated with the reversible insertion of Li ions into the Li_xMn₂O₄ phase accompanied by the formation of LiMn₂O₄. The symmetrical redox peaks indicate the highly reversible insertion/extraction of Li ions into/from the LiMn₂O₄. Fig. 2(b) shows the discharge and charge profiles of the LiMn₂O₄ at a current density of 20 mA/g in the voltage range of 3.0-4.3 V (vs. Li⁺/Li). Two pairs of voltage platform are observed during the charging and discharging, which are consistent with the CV curves. The LiMn₂O₄ electrode delivers a high initial charge capacity of 221.5 mAh/g, but a low discharge capacity of 94.1 mAh/g at 20 mA/g in the first cycle, which could be attributed to the formation of a cathode solid electrolyte interface (SEI) film and extraction of excess Li ions in the first charge cycle [27-29]. In the subsequent cycles, the irreversible charge capacity decreases, while the Coulombic efficiency increases, which indicates that the SEI film is formed mainly in the first cycle. A

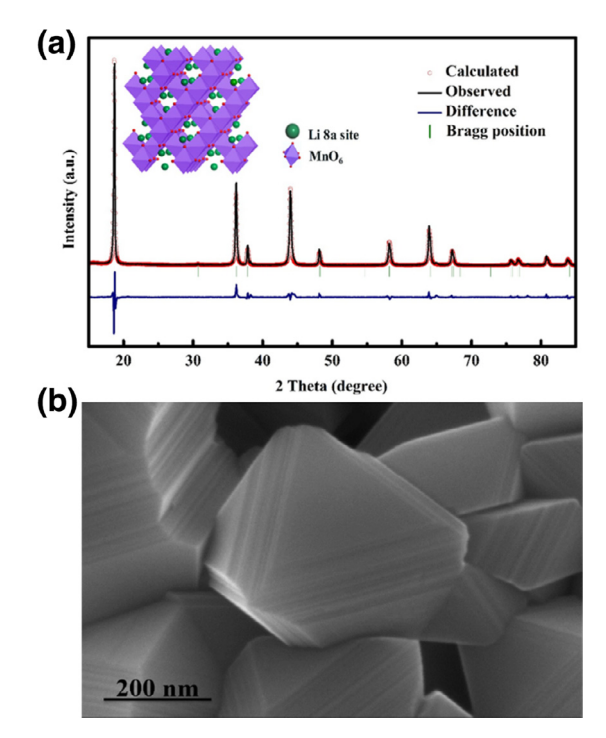


Fig. 1. (a) Rietveld refinement of the $LiMn_2O_4$ cathode. Inset: schematic of the $LiMn_2O_4$ crystal structure. (b) SEM image of the pristine $LiMn_2O_4$.

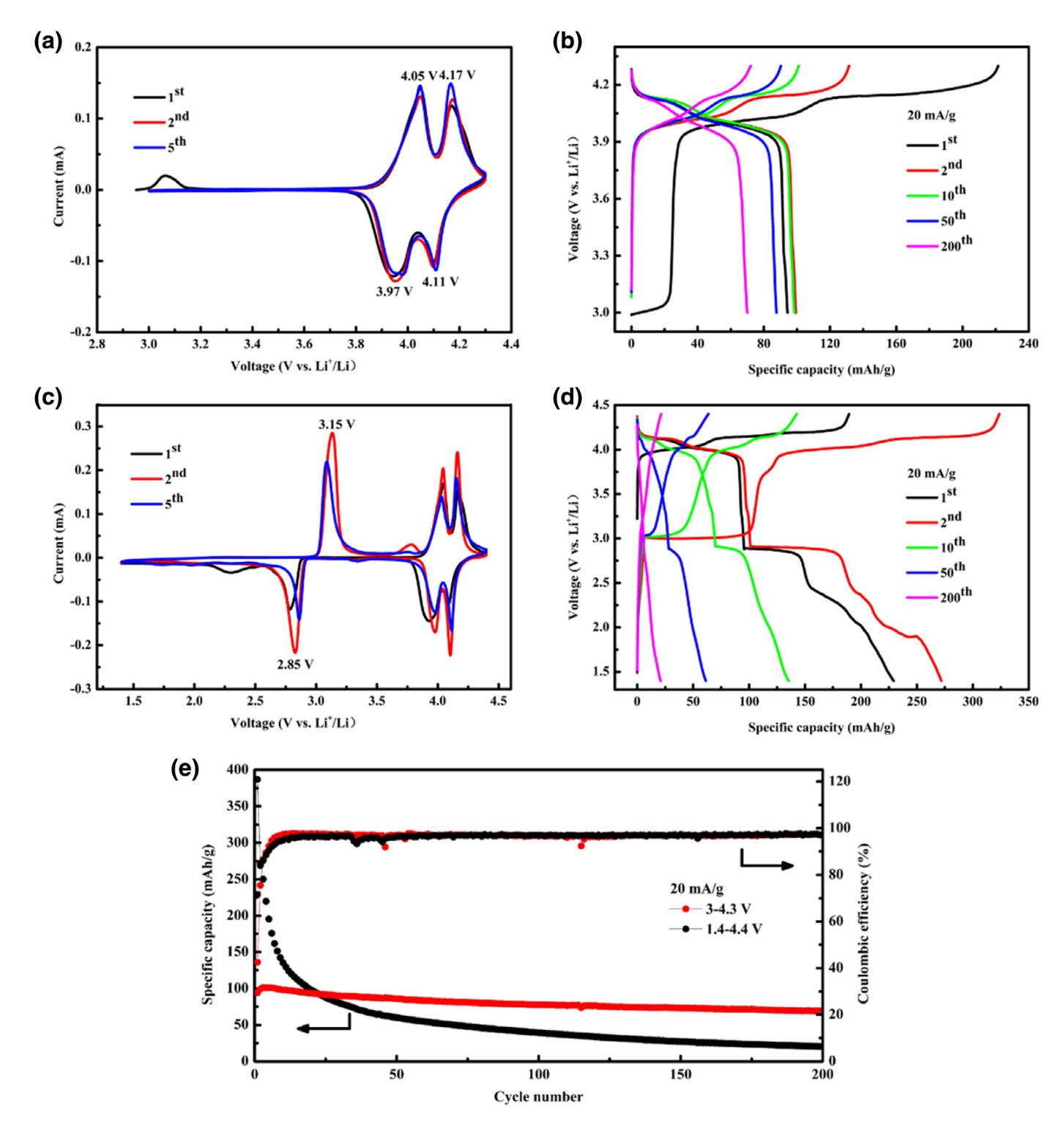


Fig. 2. (a, c) Cyclic voltammograms and (b, d) galvanostatic charge–discharge curves of the $LiMn_2O_4$ in the ranges of 3.0–4.3 and 1.4–4.4 V (vs. Li^+/Li), respectively. (e) Cycling performances and Coulombic efficiencies of the $LiMn_2O_4$ at $20\,mA/g$ in the different voltage ranges.

voltage plateau occurs at ${\sim}3.0\,V$ (vs. Li⁺/Li) in the first charge profile, which could be attributed to the self-discharge in some batteries before cycling [28,30]. We measure two cells in the range of 3.0–4.3 V (vs. Li⁺/Li) at 200 mA/g, one with self-discharge and one without self-discharge (Fig. S2). The results suggest that the cycling stabilities of the two cells are similar, which demonstrates that the small self-discharge does not accelerate the capacity fading.

Notably, a new pair of redox peaks is observed in the extended voltage window of 1.4-4.4 V (vs. Li⁺/Li) (Fig. 2c). The new reduction peak at 2.85 V (vs. Li⁺/Li) and oxidation peak at 3.15 V (vs. Li+/Li) originate mainly from the phase transformation of LiMn₂O₄ to Li₂Mn₂O₄. The corresponding voltage plateaus are observed in the charge and discharge profiles (Fig. 2d), which is in good agreement with the CV curves. The LiMn2O4 electrode exhibits a largely improved specific capacity compared to that in the range of 3.0-4.3 V (vs. Li+/Li) and delivers a high discharge capacity of 229.1 mAh/g in the first cycle. The electrochemical properties of the cells cycled in the ranges of 3.0-4.3 and 1.4-4.4 V (vs. Li+/Li) show irreversible capacity losses in the first two cycles, which could be attributed to the formation of a passivating SEI layer on the surface. Consequently, the charge capacity in the second cycle in the range of 3.0-4.3 V (vs. Li+/Li) is only 131.3 mAh/g, which is considerably lower than that in the first cycle. In the range of 1.4-4.4V (vs. Li⁺/Li), the charge capacity in the second cycle is larger than 220 mAh/g, which is even larger than that in the first cycle. This implies the formation of a new SEI layer. This phenomenon may be attributed to the formation of cracks, which lead to the fresh surface exposed to the electrolyte, as shown in Fig. S3. However, the high capacity of the LiMn₂O₄ electrode is achieved at the expense of the cycling stability. Fig. 2(e) shows the cycling performances of the LiMn₂O₄ electrode at 20 mA/g in the two different voltage windows. The LiMn₂O₄ electrode exhibits a faster trend of capacity decay in the range of 1.4-4.4 V (vs. Li⁺/Li) than that in the range of 3.0-4.3 V (vs. Li⁺/Li), with capacity loss rates of 91.13% and 26.67% after 200 cycles, respectively. Fig. S4 shows the long-term cycling performances of the LiMn₂O₄ electrode at 200 mA/g in the two different voltage windows. The LiMn₂O₄ electrode cycled in the range of 3.0-4.3 V (vs. Li+/Li) exhibits a good capacity retention of 63.16% after 600 cycles, while the LiMn₂O₄ electrode cycled in the range of 1.4-4.4 V (vs. Li+/Li) exhibits a significant capacity decay with a low retention of 5,27% after 600 cycles. Based on the above analysis, the phase transition of the cubic LiMn₂O₄ to the tetragonal Li₂Mn₂O₄ leads to the fast capacity decay of the electrode. Furthermore, Fig. S5 shows the cycling stability of the $LiMn_2O_4$ in the voltage range of 2.5–3.6 V (vs. Li⁺/Li) where only the plateau around 3.0 V (vs. Li⁺/Li) is involved. Only the phase transition of the cubic LiMn₂O₄ to the tetragonal Li₂Mn₂O₄ is observed in this voltage window. The specific capacity of the LiMn₂O₄ continuously decreases, with a capacity retention of only 26.47% after 100 cycles. In contrast, the LiMn₂O₄ exhibits a good capacity retention of 82.57% after 100 cycles in the range of 3.0–4.3 V (vs. Li⁺/Li) (Fig. 2e). Consequently, the phase transition of the cubic LiMn₂O₄ to the tetragonal Li₂Mn₂O₄ significantly reduces the structural stability and leads to the fast capacity decay.

Figs. 3 and S6 show SEM images of the $LiMn_2O_4$ after 20 cycles at $20\,mA/g$ in different voltage ranges. In the range of 3.0– $4.3\,V$ (vs. Li^+/Li), the surface of representative particles is smooth, and no signs of intergranular cracks are observed (Figs. 3a and S6a). However, in the range of 1.4– $4.4\,V$ (vs. Li^+/Li), the surface of typical particles is covered with intergranular cracks (Figs. 3b and S6b). The intergranular cracks increase the contact area of the fresh surface with the electrolyte and thereby the $LiMn_2O_4$ electrode can deliver a higher charge capacity owing to the formation of the SEI layer on the new fresh surface [14,31–33].

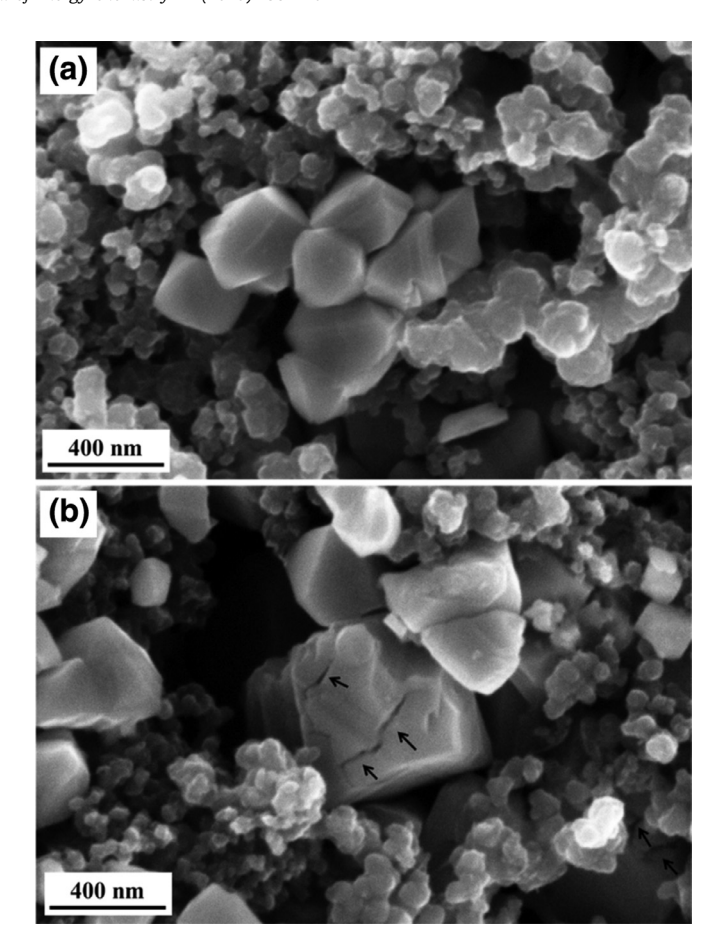


Fig. 3. SEM images of the $LiMn_2O_4$ after 20 cycles in the ranges of (a) 3.0–4.3 and (b) 1.4–4.4 V (vs. Li^+/Li). The cracks are outlined by the black arrows (b).

Operando XRD was performed to reveal the structural evolution of the LiMn₂O₄ during the cycling (1–100 cycles) in the range of 3.0-4.3 V (vs. Li⁺/Li), as shown in Fig. 4. Four characteristic peaks of spinel $Li_xMn_2O_4$ are observed in the 2θ scan range (Fig. 4a and b). During the first charge, all diffraction peaks shift to larger angles in a continuous manner, which suggests the extraction of Li ions from the LiMn₂O₄. Accordingly, the calculated lattice constant decreases from 8.246 Å to 8.082 Å, which is attributed to the structural changes in Li_xMn₂O₄ during the delithiation. During the first discharge, the peaks gradually shift to smaller angles, which corresponds to the insertion of Li ions into Li_xMn₂O₄. Accordingly, the lattice parameter increases from 8.082 Å to 8.232 Å. The evolution of peak positions and lattice parameter in the subsequent cycles (2nd, 10th, 30th, 60th, and 100th) follows that in the first cycle. With respect to the first few cycles, the (111) peak (at $2\theta = 18.69^{\circ}$) is broader after ten cycles (Fig. 4a and b). The lattice parameter of each cycle has the same change tendency. All XRD patterns indicate that the crystallinity of the LiMn₂O₄ electrode is maintained during the deintercalation/intercalation of Li⁺ although the diffraction peaks become broader [18]. The peak broadening is attributed mainly to the decrease in grain size. However, a quantitative capacity retention analysis showed that a high-voltage cycling induces intragranular cracking [14]. The intragranular cracks grow throughout the grain and generate isolated lamellas [13]. In addition, the (400) peak (at $2\theta = 43.92^{\circ}$) splits into two peaks during the first charge, which shows the two-phase coexistence in this stage, as shown in Fig. S7. This phenomenon gradually becomes apparent with the increase in number of cycles, although it appears to occur in the first cycle. This result shows that the

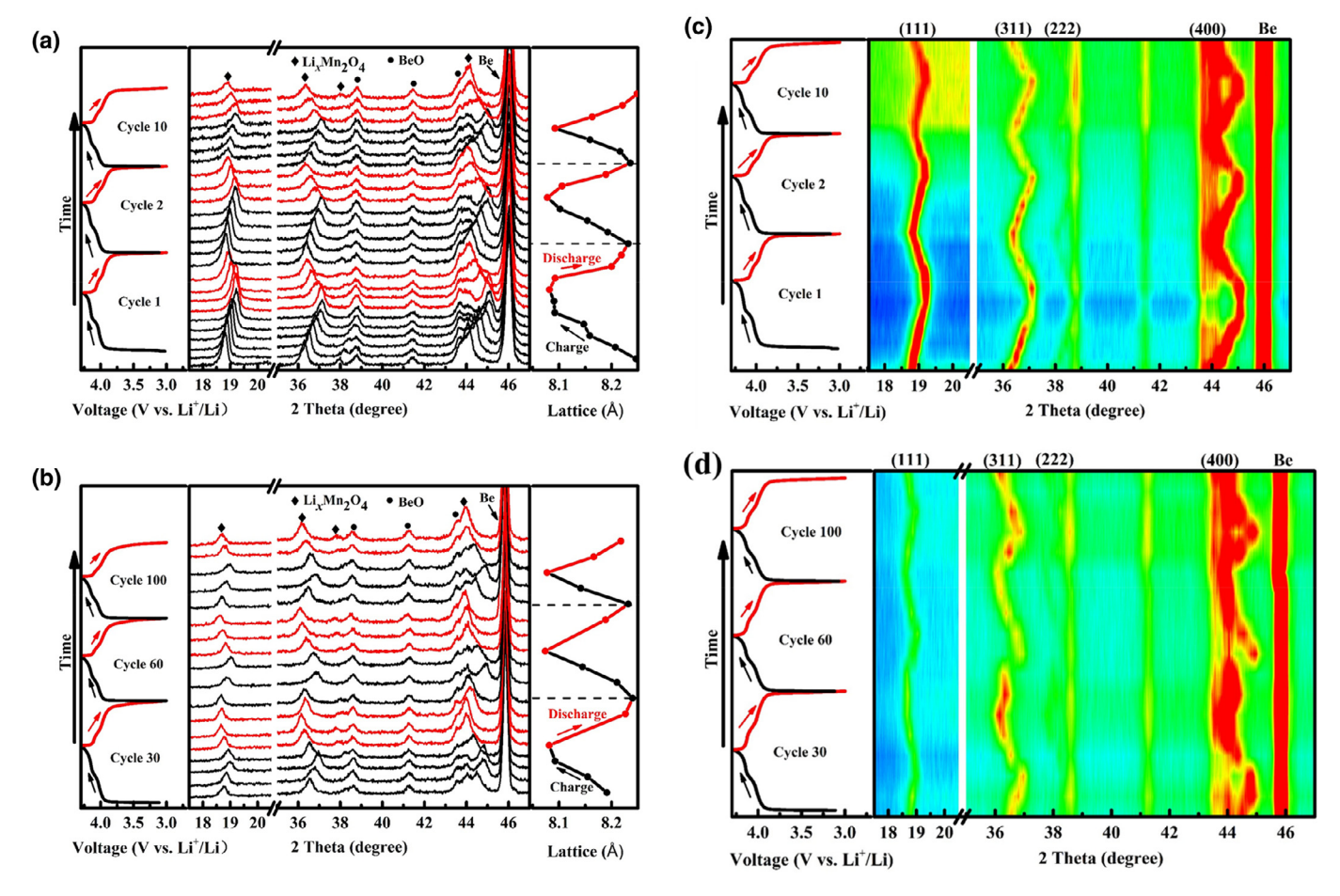


Fig. 4. (a, b) Operando XRD patterns of the $LiMn_2O_4$ cathode in the different cycles in the range of 3.0-4.3 V (vs. Li^+/Li) at 20 mA/g. (c, d) Contour plots of the operando XRD patterns in (a, b), respectively. The charge/discharge curves and variations in lattice parameters are also shown.

intragranular cracks originate from the two-phase coexistence of the material upon delithiation/lithiation. The intragranular cracks originate from parts of individual grains and gradually propagate during the cycling. Furthermore, the cell exhibits an excellent cycling stability in the range of 3.0–4.3 V (vs. Li⁺/Li) (Fig. 2e). If only the effect of intragranular cracks on the capacity fading is considered for the voltage range of 3.0–4.3 V (vs. Li⁺/Li), they form in the grain interior but do not easily extend to the surface of the particle owing to the SEI film protection. Fig. 4(c and d) shows the contour plots corresponding to the operando XRD results, which illustrate the changes in characteristic peaks and structural evolution.

To investigate the capacity fading mechanism during the cycling in the voltage range of 1.4–4.4V (vs. Li^+/Li), the operando XRD patterns of the $LiMn_2O_4$ are analyzed (Fig. 5). As shown in Fig. 5(a), the XRD patterns acquired in the voltage range of 3.0–4.3V (vs. Li^+/Li) in the first cycle are consistent with those in Fig. 4(a). During the further discharge to 1.4V (vs. Li^+/Li), the (111) peak splits into two peaks, which corresponds to the appearance of the two-phase coexistence region, which is associated with the phase transition of the cubic $LiMn_2O_4$ to the tetragonal $Li_2Mn_2O_4$ [4]. The diffraction peaks corresponding to the two-phase coexistence region are presented in Fig. 6(a). New peaks are observed at 18.34° , 32.98° , 36.76° , 37.18° , 38.81° , and 45.26° , which correspond to the (101), (103), (211), (202), (004), and (220) planes of $Li_2Mn_2O_4$, respectively. The cubic $LiMn_2O_4$ transforms to the

tetragonal Li₂Mn₂O₄ at the end of the 2.85 V (vs. Li⁺/Li) platform during the discharging, which returns to the cubic phase entirely at the end of the 3.05 V (vs. Li⁺/Li) platform during the charging. In the second cycle, the peak evolution and phase transition of the electrode are analogous to those in the first cycle. As shown in Fig. 5(a), in the 10th cycle, the (111) peak also splits into two peaks upon charging to 4.0 V (vs. Li⁺/Li), which is different from the case in the first two cycles. To clarify the constituent phases, the corresponding XRD pattern is presented in Fig. 6(b), which shows the coexistence of the cubic $LiMn_2O_4$ and λ -MnO₂. Notably, a threephase coexistence is observed around 44°, which is not observed in the voltage window of 3.0-4.3 V (vs. Li+/Li). This distinct phenomenon may be related to the formation of intergranular cracks. Upon the cycling in the voltage window of 3.0-4.3 V (vs. Li⁺/Li), the volume shrinkage and expansion corresponding to the delithiation/lithiation are reversible and generally referred to as lattice breathing. The shrinkage/expansion processes lead to the formation of intragranular cracks, which originate from parts of the individual particles and subsequently propagate during the electrochemical cycling. Nonetheless, these intragranular cracks are not exposed to the electrolyte and less new passivating SEI layers are formed in subsequent cycles. Upon the cycling in the voltage window of 1.4-4.4 V (vs. Li+/Li), the severe volume expansion during the phase transition from the cubic LiMn₂O₄ to the tetragonal Li₂Mn₂O₄ can destroy the SEI layer and lead to the formation of intergranular cracks at the grain surface. The fresh surface obtained

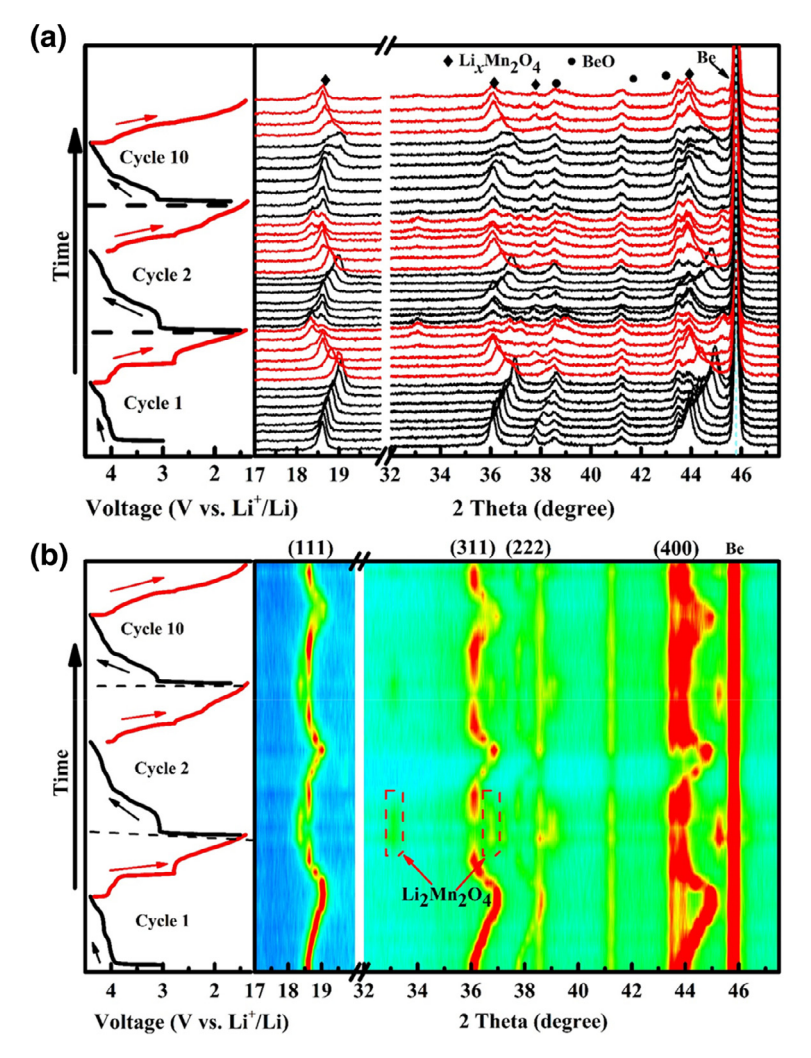


Fig. 5. (a) Operando XRD patterns of the $LiMn_2O_4$ in the different cycles in the range of 1.4–4.4 V (vs. Li^+/Li) at 20 mA/g. (b) Contour plot of the operando XRD patterns in (a). The charge/discharge profiles are also shown for reference. The black and red lines represent the charging and discharging, respectively.

upon the formation of intergranular cracks is then exposed to the electrolyte and thus a new SEI layer must be formed. The intergranular cracks initiate from the grain surface and extend to the interior during the repeated charge/discharge cycles, which leads to the pulverization of electrode materials and detachment from the current collector. This may rationalize the coexistence of the cubic LiMn₂O₄ and λ -MnO₂ as well as the three-phase coexistence. Additionally, Fig. 5(b) shows the contour plot corresponding to the operando XRD results, which illustrates the changes in characteristic peaks and structural evolution in the voltage window of 1.4–4.4 V (vs. Li⁺/Li).

Fig. 7 shows the volume changes of the $LiMn_2O_4$ during the delithiation/lithiation. In the range of 3.0–4.3 V (vs. Li^+/Li), the (111) peak shifts to larger angles during the charging and returns during the discharging (Fig. 7a). In the range of 1.4–4.4 V (vs. Li^+/Li), the (111) peak exhibits the same trend but the amplitude of the shift is larger than that in the range of 3.0–4.3 V (vs. Li^+/Li) (Fig. 7a and b). Based on the operando XRD results in Figs. 4 and 5, the lattice parameters of the involved phases during the first charge/discharge are calculated and presented in Tables S1 and S2. The volume of the unit cell changes with the shift of the diffraction peaks. As shown in Fig. 7(c), in the range of

3.0-4.3 V (vs. Li+/Li), the volume of the unit cell decreases from 560.78 to 527.89 Å³ during the first charge and then increases to 555.15 Å³ in the first discharge. The maximum volume change is approximately 5.87%, which demonstrates the excellent reversibility in this voltage range. As shown in Fig. 7(d), the volume of the unit cell increases from 524.44 to 592.08 Å³ during the first discharge to 1.4 V (vs. Li⁺/Li). The volume change (12.90%) is accompanied by the phase transition of the cubic λ -MnO₂ to the tetragonal Li₂Mn₂O₄. As shown in Fig. S8, the LiMn₂O₄ model contains 56 atoms (8 lithium, 16 manganese, and 32 oxygen atoms) in the unit cell, while the Li₂Mn₂O₄ model contains 32 atoms (8 lithium, 8 manganese, and 16 oxygen atoms). Ohzuku et al. [4] used the equations $a_{\rm T} = a_{\rm C}/\sqrt{2}$ and $c_{\rm T} = a_{\rm C}$ to convert the cubic unit cell parameter a_C into the tetragonal unit cell parameters a_T and c_T . The conversion between the cubic and tetragonal unit cell parameters follows the equation $V_T = 0.5V_C$, and thus we double the unit cell volume of the tetragonal Li₂Mn₂O₄ model to compare the volume change. This is consistent with the indexing lattice parameters shown in Table S2, and thus the volume change corresponding to the extraction/insertion of Li ions from/into LiMn2O4 is very similar. The volume change of the unit cell in the range of 3.0-4.3 V (vs. Li+/Li) is considerably smaller than that in the range of

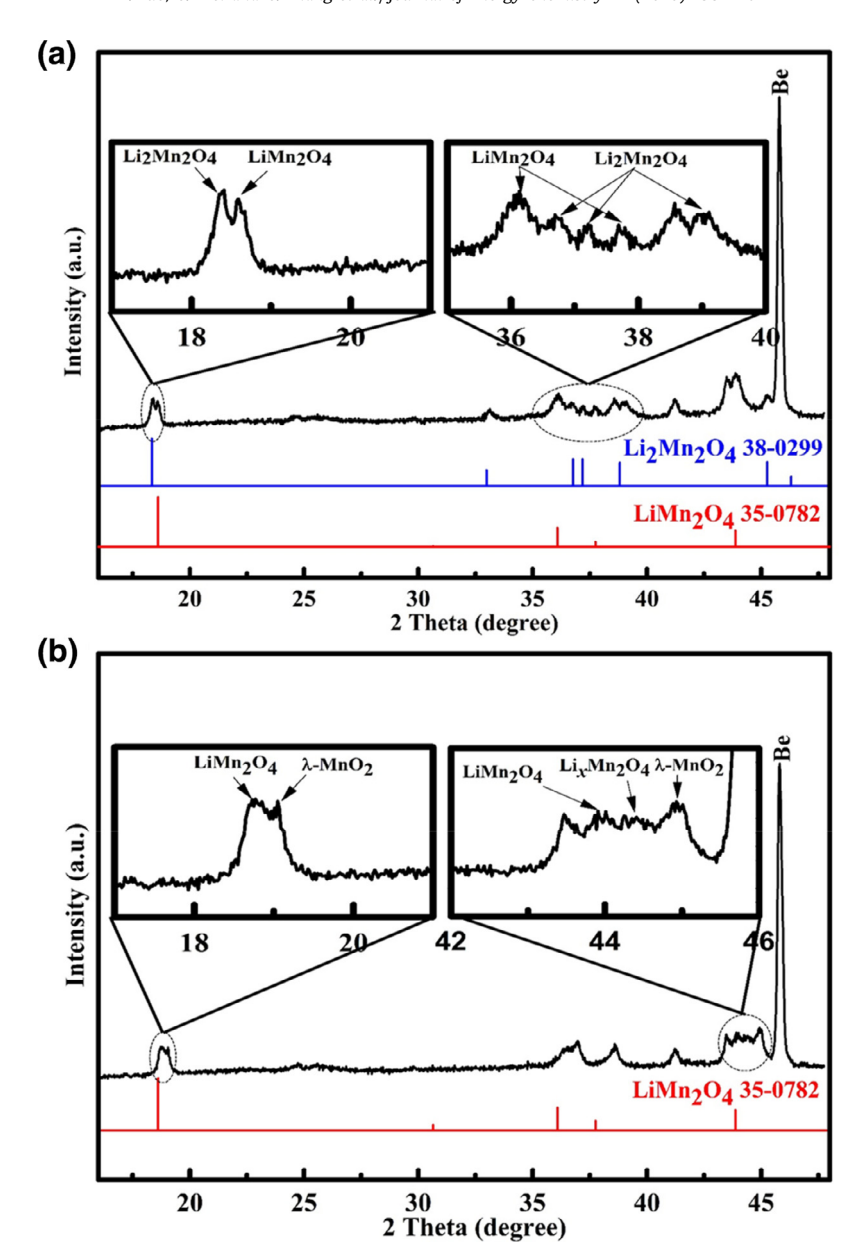


Fig. 6. Operando XRD patterns of the $LiMn_2O_4$ (a) at 2.7 V (vs. Li^+/Li) during the first discharge and (b) at 4.1 V (vs. Li^+/Li) during the 10th charge in the voltage window of 1.4–4.4 V (vs. Li^+/Li).

 $1.4\text{--}4.4\,\text{V}$ (vs. Li⁺/Li). The volume changes in the different voltage ranges are consistent with the above discussion about the cracks. The LiMn₂O₄ cycled in the range of 1.4–4.4 V (vs. Li⁺/Li) exhibits a more severe volume change than that in the range of 3.0–4.3 V (vs. Li⁺/Li), which leads to intergranular cracks and accelerates the capacity degradation.

4. Conclusions

The spinel $LiMn_2O_4$ cathode exhibited different charge/discharge behaviors and electrochemical properties (specific capacity, cycling stability) for Li storage in the voltage windows of 3.0–4.3 and 1.4–4.4 V (vs. Li^+/Li). The operando XRD elucidated

the phase evolution of the $LiMn_2O_4$ cathode and degradation mechanisms of the electrochemical performances in the different voltage windows. In the range of 3.0–4.3 V (vs. Li^+/Li), the charging and discharging were associated with the reversible extraction and insertion of Li^+ , accompanied by the small volume change of 5.87%. In the range of 1.4–4.4 V (vs. Li^+/Li), the other voltage plateau around 2.8 V (vs. Li^+/Li) was correlated with the phase transformation of the cubic $LiMn_2O_4$ to the tetragonal $Li_2Mn_2O_4$, which led to the formation of cracks as well as the performance degradation. Moreover, the volume change reached 12.90% during the first discharge. These findings provide useful information for the development of advanced electrode materials for LIBs.

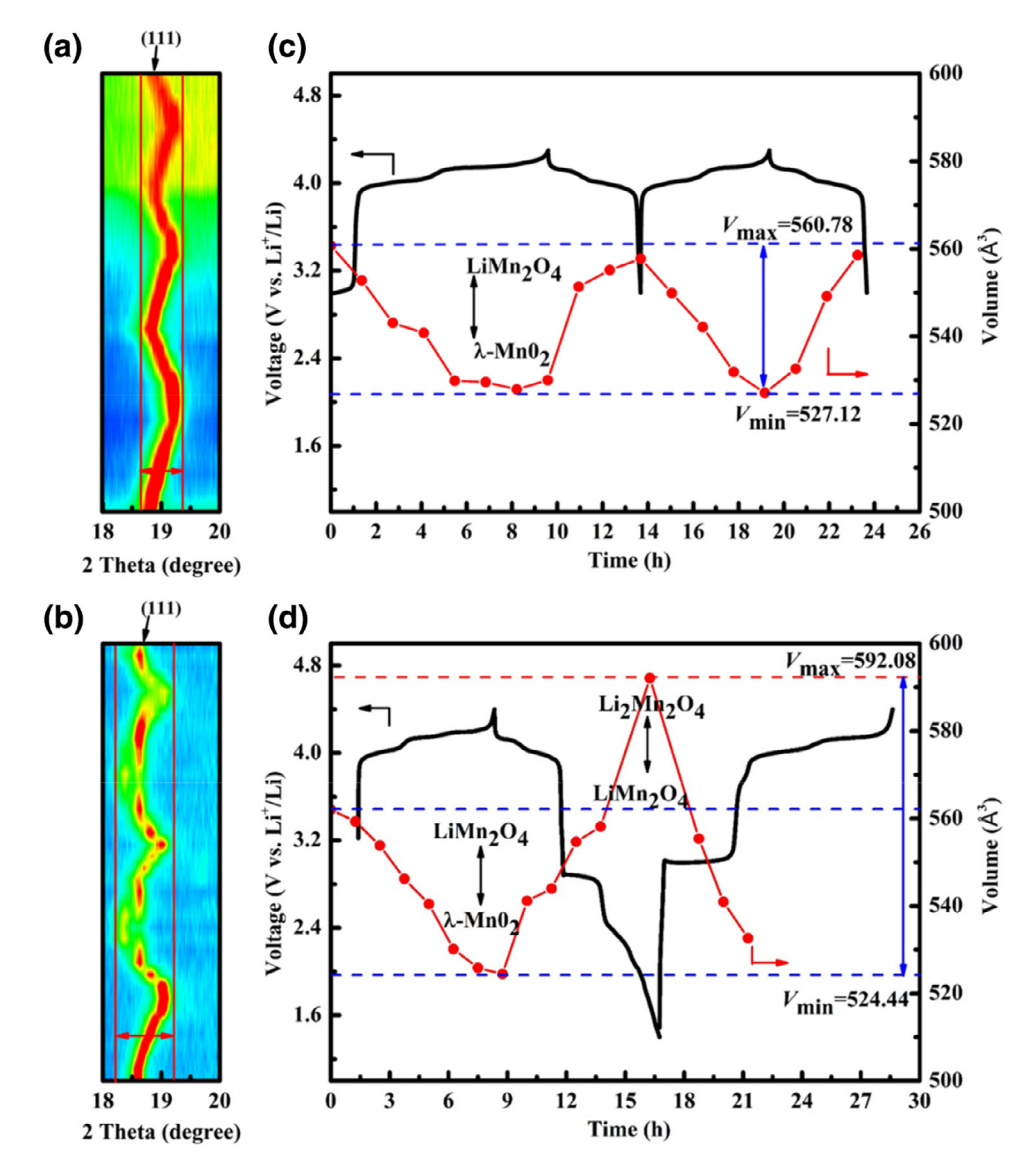


Fig. 7. Contour plots of the (111) peak evolutions of the LiMn₂O₄ during the charging/discharging in the different voltage ranges of (a) 3.0–4.3 and (b) 1.4–4.4 V (vs. Li⁺/Li) at 20 mA/g. Voltage profiles (black) and corresponding volume changes (red) of the LiMn₂O₄ during the charging/discharging in the ranges of (c) 3.0–4.3 and (d) 1.4–4.4 V (vs. Li⁺/Li) at 20 mA/g. V_{max} and V_{min} are the maximum and minimum cell volumes, respectively.

Acknowledgments

The authors gratefully acknowledge the financial support by the National Natural Science Foundation of China (51871133, 51671115) and support by the Department of Science and Technology of the Shandong Province for the Young Tip-Top Talent Support Project.

Supplementary materials

Supplementary material associated with this article can be found, in the online version, at doi:10.1016/j.jechem.2019.09.011.

References

- [1] J.B. Dunn, L. Gaines, J.C. Kelly, C. James, K.G. Gallagher, Energy Environ. Sci. 8 (2015) 158–168.
- [2] X. Feng, M. Ouyang, X. Liu, L. Lu, Y. Xia, X. He, Energy Storage Mater. 10 (2018) 246–267.
- [3] C.Y. Ouyang, S.Q. Shi, Z.X. Wang, H. Li, X.J. Huang, L.Q. Chen, EPL 67 (2004) 28–34.
- [4] T. Ohzuku, M. Kitagawa, T. Hirai, J. Electrochem. Soc. 137 (1990) 769-775.

- [5] K.F. Chiu, H.C. Lin, K.M. Lin, C.C. Chen, J. Electrochem. Soc. 153 (2006) A1992–A1997.
- [6] K. Ragavendran, H. Xia, P. Mandal, A.K. Arof, Phys. Chem. Chem. Phys. 19 (2017) 2073–2077.
- [7] W.W. Liu, D. Wang, Z. Wang, J. Deng, W.M. Lau, Y. Zhang, Phys. Chem. Chem. Phys. 19 (2017) 6481–6486.
- [8] B. Qin, S. Zhang, Z. Hu, Z. Liu, J. Zhang, J. Zhao, J. Xiong, G. Cui, Ionics (Kiel) 23 (2017) 1399–1406.
- [9] F. Schipper, P. Nayak, E. Erickson, S. Amalraj, O. Srur-Lavi, T. Penki, M. Talianker, J. Grinblat, H. Sclar, O. Breuer, C. Julien, N. Munichandraiah, D. Kovacheva, M. Dixit, D. Major, B. Markovsky, D. Aurbach, Inorganics 5 (2017) 32.
- [10] Y. Ruan, X. Song, Y. Fu, C. Song, V. Battaglia, J. Power Sources 400 (2018) 539–548.
- [11] R. Moroni, M. Borner, L. Zielke, M. Schroeder, S. Nowak, M. Winter, I. Manke, R. Zengerle, S. Thiele, Sci. Rep. 6 (2016) 30109.
- [12] D.J. Miller, C. Proff, J.G. Wen, D.P. Abraham, J. Bareño, Adv. Energy Mater. 3 (2013) 1098–1103.
- [13] K. Wang, P. Yan, M. Sui, Nano Energy 54 (2018) 148-155.
- [14] P. Yan, J. Zheng, M. Gu, J. Xiao, J.G. Zhang, C.M. Wang, Nat. Commun. 8 (2017) 14101
- [15] H. Gwon, D.H. Seo, S.W. Kim, J. Kim, K. Kang, Adv. Funct. Mater. 19 (2009) 3285–3292.
- [16] P.H. Lee, S.H. Wu, W.K. Pang, V.K. Peterson, J. Power Sources 374 (2018) 31–39.
- [17] W. Yang, J. Wang, C. Si, Z. Peng, J. Frenzel, G. Eggeler, Z. Zhang, J. Mater. Chem. A 3 (2015) 17811–17819.

- [18] R. Robert, P. Novák, J. Electrochem. Soc. 162 (2015) A1823-A1828.
- [19] D. Wang, X. Wu, Z. Wang, L. Chen, J. Power Sources 140 (2005) 125–128.
 [20] F.P. McGrogan, S.N. Raja, Y.-M. Chiang, K.J. Van Vliet, J. Electrochem. Soc. 165 (2018) A2458-A2466.
- [21] Y. Sharma, N. Sharma, G.V. Subba Rao, B.V.R. Chowdari, Adv. Funct. Mater. 17 (2007) 2855–2861.
- [22] J.M. Tarascon, E. Wang, F.K. Shokoohi, W.R. McKinnon, S. Colson, J. Electrochem. Soc. 138 (1991) 2859–2864.
- [23] Y. Zhao, J. Feng, X. Liu, F. Wang, L. Wang, C. Shi, L. Huang, X. Feng, X. Chen, L. Xu, M. Yan, Q. Zhang, X. Bai, H. Wu, L. Mai, Nat. Commun. 5 (2014) 4565.
- [24] X. Wei, X. Wang, Q. An, C. Han, L. Mai, Small Methods (2017) 1700083.

- [25] J. Lu, T. Wu, K. Amine, Nat. Energy 2 (2017) 17011.
- [26] X. Hua, R. Robert, L.S. Du, K.M. Wiaderek, M. Leskes, K.W. Chapman, P.J. Chupas, C.P. Grey, J. Phys. Chem. C 118 (2014) 15169-15184.
- [27] J.B. Goodenough, Y. Kim, Chem. Mater. 22 (2010) 587–603.
 [28] S.S. Zhang, K. Xu, T.R. Jow, J. Electrochem. Soc. 149 (2002) A1521–A1526.
- [29] X. Zhou, R.K. Guduru, P. Mohanty, J. Mater. Chem. A 1 (2013) 2757–2761.
 [30] F. Wu, G. Yushin, Energy Environ. Sci. 10 (2017) 435–459.
- [31] K. Rhodes, R. Meisner, Y. Kim, N. Dudney, C. Daniel, J. Electrochem. Soc. 158 (2011) A890–A897.
- [32] H.H. Ryu, K.J. Park, C.S. Yoon, Y.K. Sun, Chem. Mater. 30 (2018) 1155–1163.
 [33] H. Liu, M. Wolf, K. Karki, Y.S. Yu, E.A. Stach, J. Cabana, K.W. Chapman, P.J. Chupas, Nano Lett. 17 (2017) 3452–3457.